

# A Hybrid Physical-Dynamic Tire/Road Friction Model<sup>1</sup>

Jingliang Li<sup>2</sup>

Visiting Ph.D. student  
e-mail: lijingliang@bit.edu.cn

Yizhai Zhang

Ph.D. student  
e-mail: yzzhang@eden.rutgers.edu

Jingang Yi<sup>3</sup>

Assistant Professor  
e-mail: jgyi@rutgers.edu

Department of Mechanical and  
Aerospace Engineering,  
Rutgers University,  
Piscataway, NJ 08854

*We present a hybrid physical-dynamic tire/road friction model for applications of vehicle motion simulation and control. We extend the LuGre dynamic friction model by considering the physical model-based adhesion/sliding partition of the tire/road contact patch. Comparison and model parameters relationship are presented between the physical and the LuGre dynamic friction models. We show that the LuGre dynamic friction model predicts the nonlinear and normal load-dependent rubber deformation and stress distributions on the contact patch. We also present the physical interpretation of the LuGre model parameters and their relationship with the physical model parameters. The analysis of the new hybrid model's properties resolves unrealistic nonzero bristle deformation and stress at the trailing edge of the contact patch that is predicted by the existing LuGre tire/road friction models. We further demonstrate the use of the hybrid model to simulate and study an aggressive pendulum-turn vehicle maneuver. The CARSIM simulation results by using the new hybrid friction model show high agreements with experiments that are performed by a professional racing car driver. [DOI: 10.1115/1.4006887]*

**Keywords:** tire/road friction, friction model, vehicle dynamics and control, aggressive maneuvers

## 1 Introduction

Tire/road interaction plays an important role for vehicle safe operation. Real-time estimation of tire/road interaction limits such as the *maximum* friction coefficients provides critical information for active safety control of “accident-free” vehicles. There are many existing research works that use vehicle dynamics and onboard sensor measurements (e.g., global positioning system (GPS)) to estimate the *instantaneous* values of the tire/road friction forces [1]. In recent years, various “smart tire” sensors are also developed to obtain the instantaneous tire/road friction coefficient through tire deformation measurements [2–4]. However, these approaches cannot be used to directly obtain the *maximum* tire/road friction information without carrying severe maneuvers, such as emergency braking. Tire/road friction models instead provide a valuable means to predict the limits of the tire/road interactions (e.g., maximum friction coefficients) without conducting severe vehicle maneuvers.

Several friction modeling approaches have been developed to capture the tire/road interactions. The empirical friction models are obtained by curve-fitting experimental data. The pseudostatic relationships between the friction coefficients and the tire slips and the slip angles are commonly obtained in experiments. The expressions in Refs. [5] and [6], also commonly referred to as the Pacejka “magic” formula, are derived empirically to capture these pseudostatic relationships from experimental data. There is no particular physical basis for the chosen equation structures in the Pacejka’s model and, therefore the word “magic” was used to name the model. The physical models (also called brush model) are discussed in Refs. [7–11]. One basic approach of the physical model is to partition the tire/road contact patch into an adhesion region and a sliding region. In the adhesion region, the interacting

forces are determined by the elastic properties of the tire rubber bristles; whereas in the sliding region, the interacting forces depend on the frictional properties of the tire/road interface. The friction forces and moments are then calculated based on such a partition. Recently, the LuGre dynamic friction models are developed and extended to capture tire/road interactions [12–19]. The LuGre dynamic friction model uses the internal friction state dynamics to describe friction characteristics between two contact rigid objects. The model is able to not only reproduce the pseudostatic relationship between the tire and the ground but also to capture the dynamic friction behaviors such as rapidly changing friction forces.

For real-time tire/road friction estimation and control, it is difficult to directly use the empirical models because these models are highly nonlinear with the model parameters. The empirical model parameters also have no physical meanings and therefore, it is difficult to be used to capture variations of physical conditions, such as wet road, etc. One attractive property of the physical models is the physical interpretation of the friction generation mechanisms and the model parameters can also be estimated or calibrated through experiments. An advantage of the LuGre dynamic friction model lies in its compact mathematical structure to produce friction characteristics. However, its model parameters represent the mechanical properties of the bristle deformation at microscale level and it is difficult to measure through experiments. Adaptive parameter estimation methods are typically used to design real-time estimation and control algorithms due to the linear model parameterization structure in the model [13,14,20]. In Ref. [19], a refined LuGre tire/road friction model is developed to capture the normal load dependence of the bristle deformation. However, similar to the results in Refs. [15–17], the model in Ref. [19] predicts nonzero bristle deformations and stresses at the trailing edges of the contact patch, which is not realistic because of zero normal loads at these locations.

The goal of this paper is to develop an integrated physical-dynamic friction model. We take advantages of the attractive properties of both the physical and the dynamic friction models [21]. Same as the physical model, we partition the contact patch into the adhesive and sliding regions. We, however, use the LuGre dynamic friction model to compute the bristle deformation within the adhesive region and combine the physical model calculation in the sliding region. We also analyze the nonlinear and normal load-dependent strain/stress distributions on the contact patch.

<sup>1</sup>The preliminary version of this paper was presented in part at the 2009 ASME Dynamic Systems and Control Conference, Hollywood, CA, USA, Oct. 12–14, 2009, and the 2010 ASME Dynamic Systems and Control Conference, Cambridge, MA, USA, Sept. 13–15, 2010.

<sup>2</sup>Present address: School of Mechanical and Vehicular Engineering, Beijing Institute of Technology, Beijing 100081, P. R. China.

<sup>3</sup>Corresponding author.

Contributed by the Dynamic Systems Division of ASME for publication in the JOURNAL OF DYNAMIC SYSTEMS, MEASUREMENT, AND CONTROL. Manuscript received June 6, 2011; final manuscript received April 24, 2012; published online October 30, 2012. Assoc. Editor: Xubin Song.

One contribution of the new model development is that the model resolves unrealistic nonzero deformation at the trailing edge of the contact patch. For the new model, we also present the physical interpretation of the model parameters. Therefore, another contribution of the development is that the new hybrid model bridges the connection of the physical model parameters with those of the LuGre dynamic models and thus enables the use of experimental measurements to enhance real-time estimation of model parameters in the LuGre model.

We demonstrate applications of the new hybrid tire/road friction model through an example of predicting vehicle motion in a pendulum-turn aggressive maneuver. During the pendulum-turn maneuver, the vehicle motion is unstable and the tire/road interaction is often in the unstable region of its characteristics due to large normal load shifting, rapidly changing velocities, and large side-slip angles [22]. The comparisons of the motion prediction by the new model with the experiments performed by a professional racing car driver provide an excellent illustrative application of the new model for vehicle control and simulation.

The remainder of the paper is organized as follows. In Sec. 2, we review some basics of the physical and the LuGre dynamic friction models. In Sec. 3, we analyze the hybrid friction model and then show some model properties in Sec. 4. One application example is presented in Sec. 5. We conclude the paper and discuss the ongoing work in Sec. 6.

## 2 Physical and LuGre Dynamic Tire/Road Friction Models

**2.1 Tire/Road Contact Kinematics.** Figure 1 illustrates the kinematics of the tire/road contact patch  $\mathcal{P}$ . For the sake of simplicity, we assume a zero tire camber angle. We assume a rectangular shape for  $\mathcal{P}$  and let  $l$  and  $w$  denote its length and width, respectively. Two coordinate systems are defined: A ground-fixed coordinate system ( $xyz$ ) and a contact patch coordinate system ( $\xi\zeta$ ) along the tire plane. The coordinate system  $\xi\zeta$  is fixed either on the road surface (for braking) or on the tire carcass (for traction) [7]. The  $\xi$ - and  $\zeta$ -axis directions are along the tire's longitudinal and lateral motions, respectively. The origin of the  $\xi\zeta$  coordinate system is located at the center point of the leading edge of  $\mathcal{P}$ .

We assume that all points at contact patch share the same linear velocity. Let  $v_{cx}$  and  $v_{cy}$  denote the longitudinal and lateral velocity magnitudes of the tire center, respectively. We define the longitudinal slip  $\lambda$  and the slip angle  $\alpha$ , respectively, as

$$\lambda = \frac{v_{cx} - r\omega}{\max\{v_{cx}, r\omega\}} = \begin{cases} \frac{v_{cx} - r\omega}{v_{cx}} & \text{braking} \\ \frac{v_{cx} - r\omega}{r\omega} & \text{traction,} \end{cases} \quad \alpha = \tan^{-1}\left(\frac{v_{cy}}{v_{cx}}\right) \quad (1)$$

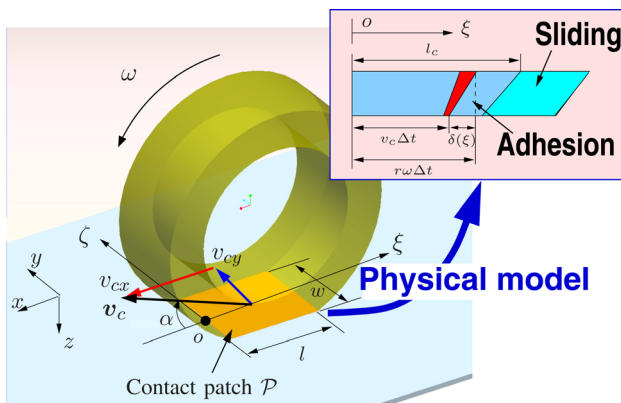


**Fig. 1 A schematic diagram of the tire motion kinematics and contact patch geometry**

where  $\omega$  is the wheel angular velocity and  $r$  is the effective tire radius.

**2.2 Physical Friction Model.** The physical (or brush) modeling approach considers the contact patch  $\mathcal{P}$  to be divided into an adhesion region and a sliding region. In the adhesion region, the interacting forces are determined by the elastic properties of the tire; whereas in the sliding region, the interacting forces depend on the adhesive properties of the tire/road interface. We define a critical length  $l_c \leq l$  such that for the adhesion region,  $0 \leq \xi < l_c$  and for the sliding region,  $l_c \leq \xi \leq l$ . We define the normalized position variables

$$x = \frac{\xi}{l}, \quad x_c = \frac{l_c}{l} \quad (2)$$

and let  $F_n$  denote the total normal load on  $\mathcal{P}$ . Similar to Ref. [7], we consider a parabolic contact pressure distribution (per unit length)  $f_n(x)$  as

$$f_n(x) = 4P_{\max} \frac{\xi}{l} \left(1 - \frac{\xi}{l}\right) = 4P_{\max} x(1-x) = 6\bar{f}x(1-x) \quad (3)$$

where  $P_{\max}$  is the maximum force per unit length (at the middle point  $x = 1/2$ ). It is straightforward to obtain that  $F_n = \int_0^l f_n(x) dx = 2/3 P_{\max} l$ , and the average pressure (per unit length)  $\bar{f} = F_n/l = 2/3 P_{\max}$ .

We consider the tire under traction and a pure longitudinal motion, namely,  $v_{cy} = 0$ . In the adhesion region  $0 \leq \xi < l_c$ , we calculate the deformation  $\delta(\xi)$  of a strip of  $\mathcal{P}$  along the  $\xi$ -axis direction at location  $\xi$  within a short time period  $\Delta t$  as

$$\delta(\xi) = r\omega\Delta t - v_{cx}\Delta t, \quad \xi = r\omega\Delta t$$

Then, we obtain

$$\delta(\xi) = \frac{r\omega - v_{cx}}{r\omega} \xi = \lambda \xi \quad (4)$$

The strain on  $\mathcal{P}$  at location  $x$  is thus  $\epsilon_a(x) = \delta(\xi)/l = \lambda x$ . We denote the tire's longitudinal stiffness per unit length is  $k_x$  and obtain the friction force for a small slip  $\lambda \ll 1$  as

$$F_{xa} = \int_0^{l_c} k_x \delta(\xi) d\xi = \frac{1}{2} k_x l^2 \lambda \quad (5)$$

Let the tire's longitudinal stiffness coefficient  $C_x$  be defined as the slope of the  $F_x$ - $\lambda$  curve at the origin, that is,  $C_x = dF_x/d\lambda|_{\lambda=0}$ . From Eq. (5) we have  $k_x = 2C_x/l^2$  and this relationship can be used to calculate  $k_x$  for a given  $C_x$ , which is obtained experimentally.

In the sliding region, we denote the sliding friction coefficient between the tire and the ground as  $\mu_x$ . The stress distribution can be obtained as  $\sigma_s(x) = \mu_x f_n(x)$  and the strain distribution is then  $\epsilon_s(x) = \mu_x f_n(x)/k_x l$ . Therefore, we summarize the stress distribution  $\sigma(x)$  on  $\mathcal{P}$  [4]

$$\sigma(x) = \begin{cases} k_x l \lambda x, & 0 \leq x < x_c, \\ 4P_{\max} \mu_x x(1-x), & x_c \leq x \leq 1 \end{cases} \quad (6)$$

and the strain distribution  $\epsilon(x)$

$$\epsilon(x) = \begin{cases} \lambda x, & 0 \leq x < x_c, \\ \frac{4P_{\max} \mu_x}{k_x l} x(1-x), & x_c \leq x \leq 1 \end{cases} \quad (7)$$

**Remark 1.** Although we present a simplified parabolic normal distribution in this paper similar to, for example, that in Ref. [7], the modeling scheme and the strain/stress calculation can be readily applied to different types of normal load distributions such as the

trapezoidal or other functional forms presented in Refs. [15–17,19].

**2.3 LuGre Dynamic Tire/Road Friction Model.** Several LuGre tire/road friction models have been developed [15–17,19]. We use and extend the distributed LuGre dynamic friction model in Ref. [19] because the model captures most comprehensive characteristics of tire/road interaction. For a pure longitudinal motion, the distributed LuGre dynamic friction model for the friction force  $F_x$  is given as

$$\frac{d\delta z(\xi, t)}{dt} = v_{rx}\hat{f}_n(\xi) - \frac{\hat{\sigma}_0|v_{rx}|}{g(v_{rx})}\delta z(\xi, t) \quad (8a)$$

$$F_x = \int_0^l \left[ \sigma_0\delta z(\xi, t) + \sigma_1 \frac{\partial\delta z(\xi, t)}{\partial t} + \sigma_2 v_{rx} \right] d\xi \quad (8b)$$

where  $\delta z(\xi, t)$  is the average rubber bristle deformation at  $\xi$ ,  $\hat{\sigma}_0 = \sigma_0/\hat{f}$ ,  $\sigma_0$ ,  $\sigma_1$ , and  $\sigma_2$  are the bristle elastic stiffness, viscous damping coefficient, and sliding damping coefficient per unit length, respectively. For relative velocity  $v_{rx} = v_{cx} - r\omega$ , we have

$$g(v_{rx}) = \mu_C + (\mu_S - \mu_C)e^{-\left(\frac{v_{rx}}{v_s}\right)^{1/2}} \quad (9)$$

where  $\mu_C$  and  $\mu_S$  are Coulomb and static friction coefficients, respectively, and  $v_s$  is the Stribeck velocity. We use a dimensionless variable  $\hat{f}_n(\xi) = f_n(\xi)/\hat{f} = 6x(1-x)$  in Eq. (8) to represent the effect of the normal load on the bristle deformation.

One of the major differences between the model (8) and those in Refs. [15–17] is the introduction of the dependence of normal load distribution  $\hat{f}_n(\xi)$  on the bristle deformation. The model also includes the normal load dependence for other model parameters [19].

Similar to the longitudinal braking/traction case, the two-dimensional distributed LuGre friction model is given as [19]

$$\frac{d\delta z_i(\xi, t)}{dt} = v_{ri}\hat{f}_n(\xi) - \frac{\hat{\sigma}_{0i}\bar{\gamma}(v_R, \mu)}{g_i^2(v_R)}\delta z_i(\xi, t) \quad (10a)$$

$$F_i = \int_0^l \left[ \sigma_{0i}\delta z_i(\xi, t) + \sigma_{1i} \frac{\partial\delta z_i(\xi, t)}{\partial t} + \sigma_{2i}v_{ri} \right] d\xi \quad (10b)$$

where  $F_i$ ,  $i = x, y$ , are the longitudinal and lateral forces, respectively

$$g_i(v_R) = \mu_{ki} = \mu_{Ci} + (\mu_{Si} - \mu_{Ci})e^{-|v_R/v_s|^{1/2}}, \quad i = x, y$$

$v_R = \sqrt{v_{rx}^2 + v_{ry}^2}$  is the magnitude of the relative velocity,  $v_{ry} = v_{cy}$  is the tire lateral relative velocity, and  $\bar{\gamma}(v_R, \mu) = \sqrt{(\mu_{kx}v_{rx})^2 + (\mu_{ky}v_{ry})^2}$ . The coupling effect of the longitudinal and lateral motions is captured through the terms  $v_R$  and  $\bar{\gamma}(v_R, \mu)$  in the model.

### 3 Hybrid Model and Steady-State Friction Forces

In this section, we present the hybrid physical-dynamic friction model and the friction force calculation at steady state. The basic idea of the hybrid physical-dynamic friction model is to use the LuGre dynamic friction model to predict the bristle deformation and stress distributions in the adhesion region of the contact patch. Meanwhile, we use the physical model-based stress distribution and the friction force calculations on the sliding region. Although for presentation clarity, we mainly focus on the development for the case where the tire is under pure longitudinal motion, the results can be extended to the coupled longitudinal/lateral motion. Similar to the other dynamic friction model developments in Refs. [15–17], we finally present a lumped hybrid tire/road friction model based on the distributed model.

**3.1 Steady-State Deformation and Stress Distributions.** The steady state we consider here refers to that the tire rubber bristle deformation  $\delta z(\xi, t)$  reaches its steady state in time, that is,  $\partial\delta z(\xi, t)/\partial t = 0$ . For Eq. (8a), we consider that

$$\frac{d\delta z(\xi, t)}{dt} = \frac{\partial\delta z(\xi, t)}{\partial\xi} \frac{d\xi}{dt} + \frac{\partial\delta z(\xi, t)}{\partial t} = \frac{\partial\delta z(\xi, t)}{\partial\xi} v_c + \frac{\partial\delta z(\xi, t)}{\partial t} \quad (11)$$

In the above equation, we use  $\dot{\xi} = v_c$  to represent the translational velocity of the particle on the road moving along  $\mathcal{P}$  during braking. We here consider the tire center is fixed and the road is moving at  $v_c$  in the opposite direction as the wheel's motion. This treatment is different with those in the previous study in Refs. [15–17,19], in which  $\dot{\xi} = r\omega$  for particles on the tire carcass.

At the steady state,  $\partial\delta z(\xi, t)/\partial t = 0$  and from Eqs. (11) and (8a), we obtain the following ordinary differential equation for  $\delta z_{ss}(\xi)$  that represents the steady-state of  $\delta z(\xi, t)$

$$\frac{d\delta z_{ss}(\xi)}{d\xi} = \lambda\hat{f}_n - \hat{a}\delta z_{ss}(\xi) \quad (12)$$

where  $\hat{a} = \hat{\sigma}_0\lambda/g(v_R)$  and  $v_R = v_{rx}$  for longitudinal motion. Solving Eq. (12) with initial condition at the leading edge  $\delta z_{ss}(0) = 0$ , we obtain

$$\begin{aligned} \delta z_{ss}(\xi) &= \int_0^\xi e^{-\hat{a}(\xi-\tau)} \lambda\hat{f}_n(\tau) d\tau \\ &= \frac{6}{l\hat{a}} \left[ -\frac{\xi^2}{l} + \left( \frac{2}{l\hat{a}} + 1 \right) \xi - \frac{1}{\hat{a}} \left( 1 + \frac{2}{l\hat{a}} \right) (1 - e^{-\hat{a}\xi}) \right] \lambda \geq 0 \end{aligned} \quad (13)$$

The deformation  $\delta z_{ss}(\xi) \geq 0$  is directly from the fact that each term in the above integration is non-negative. Letting

$$x_a = l\hat{a} = \frac{l\hat{\sigma}_0\lambda}{g(v_R)} \geq 0 \quad (14)$$

we then rewrite (13) as

$$\begin{aligned} \delta z_{ss}(x) &= \frac{6g(v_R)}{\hat{\sigma}_0} \left[ -x^2 + \left( 1 + \frac{2}{x_a} \right) \left( x - \frac{1 - e^{-x_a x}}{x_a} \right) \right] \\ &= \frac{6g(v_R)}{\hat{\sigma}_0} [-x^2 + x + h(x; x_a)] \end{aligned} \quad (15)$$

where function

$$h(x; x_a) = \frac{2}{x_a}x - \frac{1}{x_a} \left( 1 + \frac{2}{x_a} \right) (1 - e^{-x_a x}) \quad (16)$$

From Eq. (13), we notice that the bristle deformation  $\delta z_{ss}(\xi)$  depends on the normal load distribution  $\hat{f}_n(\xi)$ . We here choose a quadratic form of  $\hat{f}_n(\xi)$  to calculate the closed-form  $\delta z_{ss}(\xi)$  and then later to explicitly show and compare analytical properties with the existing results by the other models. It is possible to demonstrate the similar mathematical properties for any general function form of  $\hat{f}_n(\xi)$ .

*Remark 2.* We can clearly see the difference between the dynamic friction model and the physical model in the case of a small tire slip  $\lambda \ll 1$ , namely,  $\hat{a} \ll 1$ . In this case, using Taylor expansion  $e^{-\hat{a}\xi} = 1 - \hat{a}\xi + \frac{1}{2}\hat{a}^2\xi^2$ , from Eq. (15) we obtain

$$\delta z_{ss}(x) = \frac{3\xi^2}{l} \lambda = 3lx^2\lambda \quad (17)$$





$$\begin{aligned}
\bar{z}(t) &= \frac{1}{l} \int_0^{l_c} \delta z_a(\xi, t) d\xi + \frac{1}{l} \int_{l_c}^l \delta z_s(\xi, t) d\xi \\
&= \frac{1}{l} \int_0^l \delta z_a(\xi, t) d\xi - \frac{1}{l} \int_{\xi_c}^l \frac{6g(v_R)}{\hat{\sigma}_0} h(x; x_a) d\xi \\
&= \frac{1}{l} \int_0^l \delta z_a(\xi, t) d\xi - z_a
\end{aligned} \quad (28)$$

where the second term in Eq. (28) is obtained as

$$\begin{aligned}
z_a &= \frac{1}{l} \int_{\xi_c}^l \frac{6g(v_R)}{\hat{\sigma}_0} h(x; x_a) d\xi = \frac{6g(v_R)}{\hat{\sigma}_0} \int_{x_c}^1 h(x; x_a) dx \\
&= -\frac{6g(v_R)}{\hat{\sigma}_0 x_a} \left[ x_c \left( 1 + x_c - \frac{2}{x_a} \right) + h(1; x_a) \right]
\end{aligned} \quad (29)$$

Taking time derivative of  $\bar{z}(t)$  in Eq. (28) and using (8), we obtain the lumped hybrid friction model

$$\dot{\bar{z}}(t) = \left( v_r - \frac{v_c}{l} z_l - \frac{\hat{\sigma}_0}{g(v_R)} z_a \right) - \frac{\hat{\sigma}_0}{g(v_R)} \bar{z}(t) \quad (30a)$$

$$F_x = (\sigma_0 \bar{z}(t) + \sigma_1 \dot{\bar{z}}(t) + \sigma_2 v_R) l \quad (30b)$$

Similar to the above case of only the longitudinal motion, we can obtain the lumped LuGre dynamic friction model for the coupled longitudinal and lateral motion and we omit the detailed development here.

#### 4 Steady-State Model Properties

In this section, we show some properties of the hybrid friction model presented in Sec. 3. These properties are helpful to reveal and understand the underlying relationship of the new model with the existing models.

First, we show the following results for function  $h(x; x_a)$  in Eq. (16).

**Property 1.** *The bristle deformation function  $h(x; x_a)$  satisfies the following properties.*

$$\begin{aligned}
\lim_{\lambda \rightarrow 0} h(x; x_a) &= \lim_{x_a \rightarrow 0} h(x; x_a) = x^2 - x, \quad \lim_{\lambda \rightarrow \infty} h(x; x_a) \\
&= \lim_{x_a \rightarrow \infty} h(x; x_a) = 0
\end{aligned}$$

for any  $0 \leq x \leq 1$ .

*Proof.* It is straightforward to see that  $\lim_{x_a \rightarrow \infty} h(x; x_a) = 0$  because  $1 - e^{-x_a x}$  and  $0 \leq x \leq 1$  are finite. When  $x_a \rightarrow 0$ , for any  $x > 0$  we have

$$\begin{aligned}
\lim_{x_a \rightarrow 0} h(x; x_a) &= \lim_{x_a \rightarrow 0} \frac{2x - [(1 - e^{-x_a x}) + (x_a + 2)xe^{-x_a x}]}{2x_a} \\
&= \lim_{x_a \rightarrow 0} \frac{e^{-x_a x}(-x) - e^{-x_a x}x + (x_a + 2)x^2 e^{-x_a x}}{2} = x^2 - x
\end{aligned}$$

For  $x = 0$ , it is easy to check that  $\lim_{x_a \rightarrow 0} h(x; x_a) = 0 = x^2 - x$ . Therefore, the properties hold.

From the above property, we obtain that the bristle deformation  $\delta z_{ss}(x)$  is zero when the tire slip  $\lambda = 0$ , namely

$$\lim_{\lambda \rightarrow 0} \delta z_{ss}(x) = \lim_{x_a \rightarrow 0} \delta z_{ss}(x) = 0$$

This represents the pure slipping case and thus no friction force is generated.

From Eq. (16) and continuity of stress distribution, we know that  $x = x_c$  is the solution of the following equation:

$$h(x; x_a) = 0 \quad (31)$$

for a given  $x_a$ . From Eq. (16), we rearrange (31) and obtain

$$\frac{2x_a x_c - x_a - 2}{2} e^{\frac{2x_a x_c - x_a - 2}{2}} = \left( -\frac{x_a}{2} - 1 \right) e^{-\frac{x_a}{2} - 1}$$

The solution of  $x_c$  given in the above equation can be conveniently written as a form of the Lambert W function [24]

$$\frac{2x_a x_c - x_a - 2}{2} = W_0 \left[ \left( -\frac{x_a}{2} - 1 \right) e^{-\frac{x_a}{2} - 1} \right] = W_0(X_a) \quad (32)$$

where

$$X_a = \left( -\frac{x_a}{2} - 1 \right) e^{-\frac{x_a}{2} - 1} \quad (33)$$

and the Lambert W function  $x = W(z)$  is the solution of the equation  $z = xe^x$  for a given  $z \in \mathbb{R}$ . The notation  $W_0(z)$  in Eq. (32) denotes the principle branch (i.e.,  $W(z) > -1$ ) of the Lambert W function  $W(z)$  [24]. We denote the other branch  $W(z) < -1$  of the Lambert W function as  $W_{-1}(z)$ . Noticing that  $x_a \geq 0$ , it is straightforward to obtain that  $X_a$  in Eq. (33) is monotonically increasing with  $x_a$  and also  $-e^{-1} \leq X_a < 0$ ; see Appendix A. From Eq. (33) and the definition of the Lambert W function, we obtain  $-x_a/2 - 1 = W_{-1}(X_a)$  because of  $-x_a/2 - 1 < -1$ . Thus, we write  $x_a$  in terms of  $X_a$  as

$$x_a = -2W_{-1}(X_a) - 2 \quad (34)$$

Using the results in Eqs. (32)–(34), we obtain  $x_c$  as

$$x_c = \frac{1}{2} + \frac{W_0(X_a) + 1}{x_a} = \frac{1}{2} - \frac{1}{2} \frac{W_0(X_a) + 1}{W_{-1}(X_a) + 1} \quad (35)$$

We are now ready to show properties of the partition location  $x_c$  of  $\mathcal{P}$ .

**Property 2.** *There exists a nontrivial  $0 < x_c \leq 1$  for nonzero slip  $\lambda > 0$ . For  $\lambda > 0$  and  $0 < x_a < +\infty$ ,  $x_c$  satisfies  $\frac{1}{2} < x_c \leq 1$ . Moreover,  $x_c$  is monotonically increasing with  $x_a$ .*

$$\lim_{x_a \rightarrow 0} x_c = 1, \quad \text{and} \quad \lim_{x_a \rightarrow \infty} x_c = \frac{1}{2} \quad (36)$$

*Proof.* See Appendix A.

With the results of Property 2, we further show the following properties.

**Property 3.** *For the normal distribution  $f_n(x)$  given in Eq. (3) on the contact patch  $0 \leq x \leq l$ , we have the following properties for the hybrid model:*

- (1) There exists a unique  $0 \leq x_c \leq 1$  such that the stress distribution  $\sigma(x)$  in Eq. (23) of the hybrid model satisfies that when  $0 \leq x \leq x_c$ ,  $\sigma_a(x) \leq \sigma_s(x)$  and  $x_c < x \leq 1$ ,  $\sigma_a(x) > \sigma_s(x)$ ;
- (2) The steady-state deformation  $\delta z_{ss}(x)$  in Eq. (22) achieves its maximum value at  $x_c$ , namely,  $x_{\max} = x_c$ .

*Proof.* See Appendix B.

In Fig. 3, we plot the steady-state deformation  $\delta z_{ss}(\xi)$  by combining the adhesive portion with the sliding portion under various slip values. It is noted that  $\sigma(\xi)$  in Eq. (23) is a combination of two portions of the stress curves. The stress  $\sigma(\xi)$  is continuously distributed across  $\mathcal{P}$ . Moreover,  $\sigma(\xi)$  reaches its maximum value at  $l_c$ . The location of the maximum stress here is consistent with the results reported in Ref. [7]. At the leading and trailing edges of  $\mathcal{P}$ , the values of  $\sigma(\xi)$  are equal to zero. These properties match the experimental results in the literature and are different from the results given by the other LuGre tire/road friction models in Refs. [15–17,19], where a nonzero bristle deformation is obtained at the trailing edge.

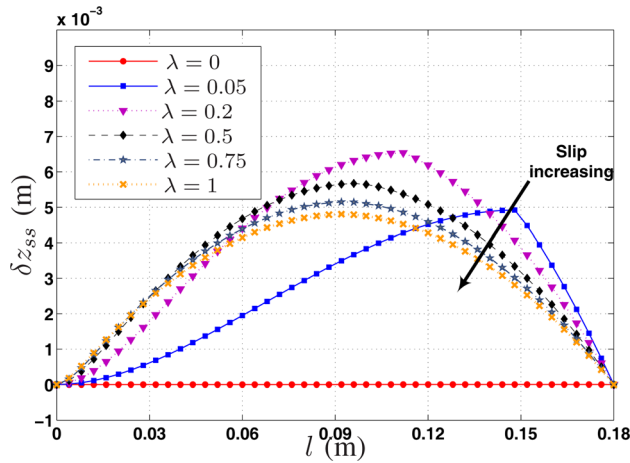


Fig. 3 Steady-state bristle deformation under various slip values

We further compare the location  $x_c$  of the hybrid model with that of the physical model. We denote  $x_c^p$  as the location of the contact patch separation point by the physical model. Using the notations given in the LuGre model and the relationship  $k_x = 2\sigma_0$ , we rewrite (6) as

$$\sigma(x) = \begin{cases} 2\sigma_0\lambda x, & 0 \leq x < x_c^p \\ 6\bar{f}g(v_R)x(1-x), & x_c^p \leq x \leq 1 \end{cases} \quad (37)$$

At  $x_c^p$ , the stresses given by the two formulations in Eq. (37) must be equal due to stress continuity and, thus we obtain

$$2\sigma_0\lambda x_c^p = 6\bar{f}g(v_R)x_c^p(1-x_c^p)$$

The above equation reduces to

$$x_c^p = 1 - \frac{1}{3}x_a \quad (38)$$

We show the following result regarding the locations of  $x_c^p$  in Eq. (38) and  $x_c$  in Eq. (35).

**Property 4.** The location of critical point  $x_c$  by the hybrid model (35) is larger than or equal to that by the physical model  $x_c^p$  in Eq. (38), namely,  $x_c \geq x_c^p$ .

*Proof.* See Appendix C.

We illustrate the results in Property 4 in Fig. 2. The separation point  $x_c^p$  of the physical model is always located ahead of that of the hybrid model  $x_c$ . Moreover, when slip  $\lambda$  increases,  $x_c^p$  increases as well and the entire contact patch becomes one sliding region as predicted by the physical model [7]. In this case, the value of  $x_a$  in Eq. (14) is large and from Eq. (16), when  $x_a \rightarrow \infty$ ,  $h(x; x_a) \rightarrow 0$ , and  $x_c \rightarrow \frac{1}{2}$ , the stress distribution  $\sigma_a(x) \rightarrow \sigma_s(x)$ , and then the entire contact patch indeed becomes one sliding region by the hybrid model. Therefore, these two models reach the same physical interpretation.

**Remark 4.** To precisely describe the above explanation for large slip values, similar to the results in Ref. [7], it is noted that the value of slip  $\lambda$  must satisfy  $1 \leq \lambda \leq 3g(v_R)/l\hat{\sigma}_0 := \lambda_S$  for non-negative  $x_c^p \geq 0$  given in Eq. (38). For a large slip  $\lambda > \lambda_S$ , the entire contact patch is under sliding by the physical model. The friction force  $F_{xs}$  by the physical model reaches its maximum value when  $\lambda = \lambda_S$ . For the hybrid model, the relationship between the friction force  $F_{xs}$  and slip  $\lambda$  by Eq. (24) is complex (through variable  $x_a$  and function  $g(v_R)$ ). As we explained in Remark 3, it is

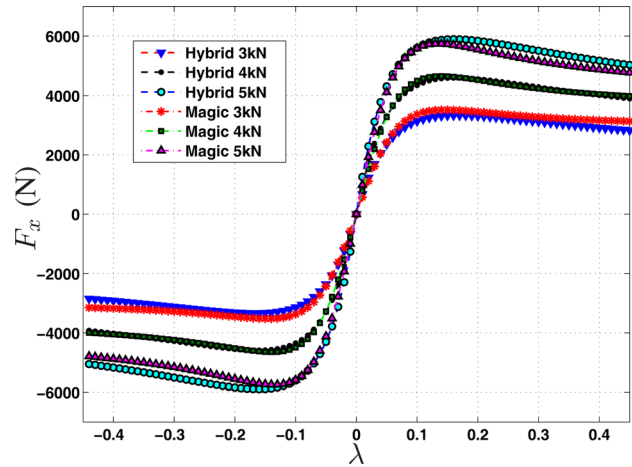


Fig. 4 Comparison results of the longitudinal force  $F_x$  of the hybrid physical-dynamic model with the Pacejka "magic" formula under various normal loads

difficult to obtain an analytical formulation for the similar slip range  $\lambda_S$  at which  $F_{xs}$  reaches its maximum value.

## 5 Application Example

In this section, we present one application example to illustrate the use of the hybrid tire/road friction model in vehicle motion simulation of a pendulum-turn aggressive maneuver.

We first compare the predictions of the hybrid friction model with these by the Pacejka "magic" formula [6]. Figure 4 shows an example of the steady-state friction force  $F_x$  as a function of  $\lambda$  with zero slip angle  $\alpha = 0$  and  $v_{cx} = 25$  m/s. The hybrid friction model parameters are obtained by comparing with experimental data and validated in the CARSIM simulation [22]. These model parameters are listed in Table 1. The comparison results of the predictions of the hybrid friction model with the Pacejka "magic" formula are also shown in Fig. 4 for various normal loads. Clearly, the hybrid model accurately predicts the friction forces given by the Pacejka "magic" formula. Although we only show the comparison results under a case of zero slip angle, we have conducted comparison studies with nonzero slip angles and the model predictions achieve the similar performance [25]. A more comprehensive comparison study is also reported in Ref. [19] for a similar LuGre dynamic friction model.

Table 1 Hybrid physical-dynamic friction model parameters

$\hat{\sigma}_{0x}$	$\hat{\sigma}_{0y}$	$\sigma_{0x}$	$\sigma_{0y}$	$\sigma_{1x}$	$\sigma_{1y}$	$\sigma_{2x}$	$\sigma_{2y}$	$\mu_{Si}$	$\mu_{Ci}$	$v_{sx}$	$v_{sy}$
209.3	54.1	290	340	0.4	0.4	0.002	0	2.24	0.74	0.71	1

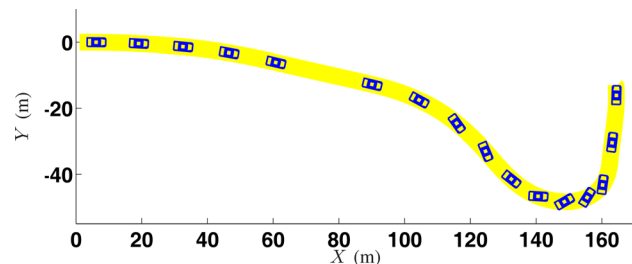


Fig. 5 A vehicle trajectory of a pendulum-turn maneuver from racing driving experiments

In the following, we discuss the use of the hybrid friction model to simulate a pendulum-turn aggressive vehicle maneuver. Pendulum-turn maneuver is a high-speed sharply cornering strategy that is used by racing car drivers [26,27]. The driving strategies during the pendulum turn include not only the coordinated actuation among braking/traction and steering, but also quickly

changing forces distribution among four tires and along the longitudinal/lateral directions at each tire. During this aggressive maneuver, the vehicle is often operated under unstable motion and the tire/road interactions are in the nonlinear unstable regions of the friction force characteristics [22]. Therefore, the pendulum-turn maneuver provides an excellent illustrative example to

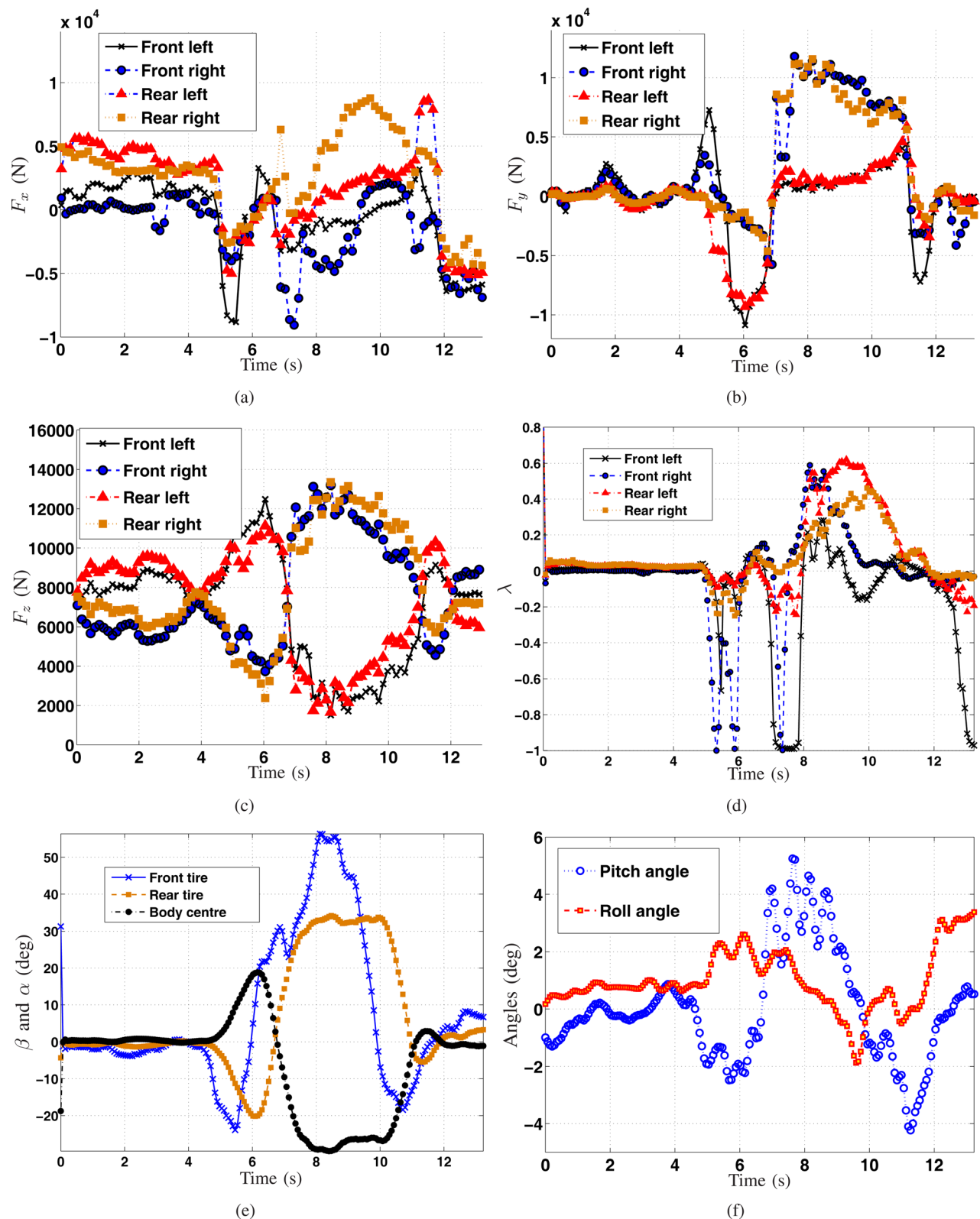


Fig. 6 Testing data at four tires. (a) Longitudinal friction forces  $F_x$ . (b) Lateral friction forces  $F_y$ . (c) Normal loads  $F_z$ . (d) Tire slip ratios  $\lambda$ . (e) Tire slip angles  $\alpha$  and vehicle side-slip angle  $\beta$ . (f) Vehicle pitch and roll angles.

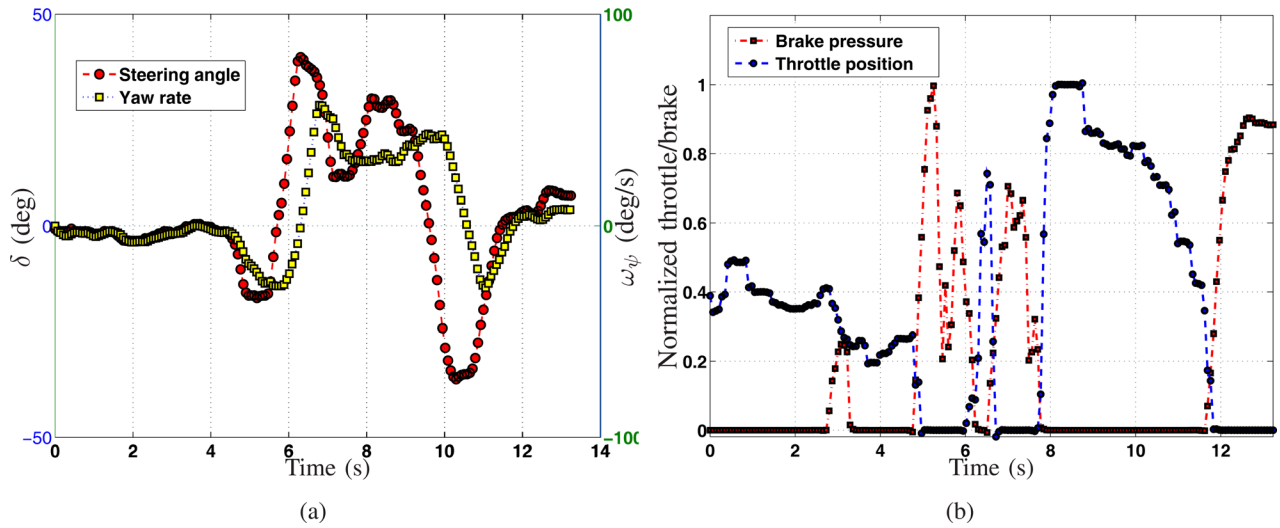


Fig. 7 Racing car driver input data. (a) Steering angle  $\delta$  and yaw rate  $\omega_\psi$ . (b) Normalized throttle/braking actuation.

demonstrate the prediction of the dynamically changing tire/road friction forces under conditions such as large normal load shifting, fast velocity change, and large side-slip angles, etc.

The pendulum-turn maneuver experiments were conducted at the Ford research facilities by professional racing car drivers. Figure 5 shows the vehicle trajectory for a sharp turn. The testing

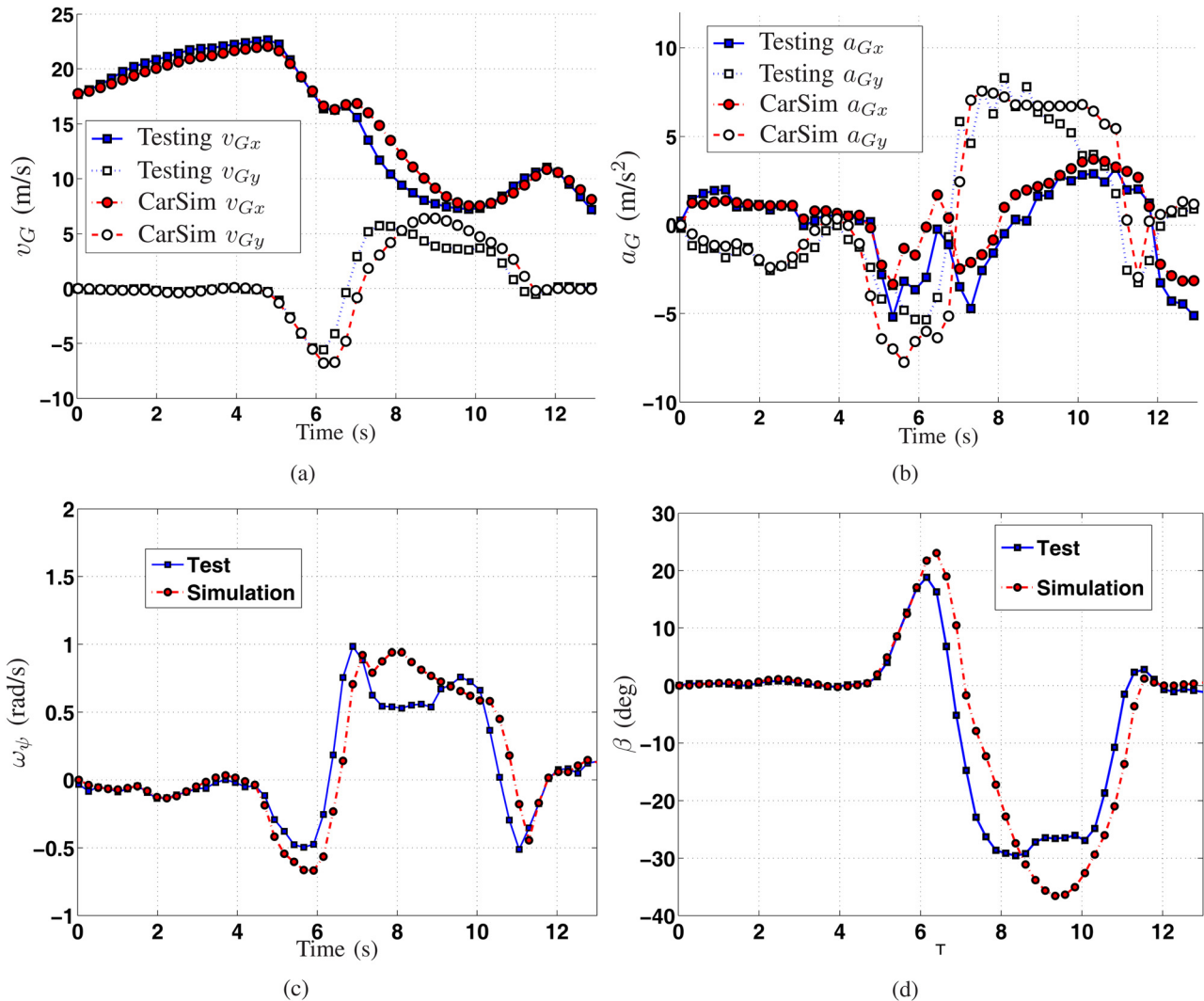


Fig. 8 Comparison of simulation results and testing data. (a) Longitudinal/lateral velocity  $v_{Gx}/v_{Gy}$ . (b) Longitudinal/lateral acceleration  $a_{Gx}/a_{Gy}$ . (c) Yaw rate  $\omega_\psi$ . (d) Vehicle side-slip angle  $\beta$ .



vehicle was a Ford Explorer SUV and the vehicle was instrumented with various sensors. Since we did not have access to GPS positioning data, we used an extended Kalman filter to estimate the vehicle's position information by fusing the acceleration information with the velocity measurements [28]. From the collected sensor measurements and vehicle parameters provided by Ford, we calculated the tire slips and slip angles and then estimated the friction forces at each tire using the hybrid physical-dynamic friction model. The detailed description of the experiments and the motion variables estimation is discussed in Ref. [22].

Figures 6(a)–6(c) show the three-directional tire/road friction forces at four tires and Figs. 6(d)–6(e) show the tire slips and the tire slip angles, respectively. The vehicle's pitch and roll angles are shown in Fig. 6(f). The driver's steering, braking/traction inputs, and the vehicle's yaw rate are shown in Fig. 7. The vehicle motion variables such as the longitudinal/lateral velocities and accelerations are shown in Fig. 8.

During the pendulum-turn maneuver, the driver first used counter-steering at the beginning of the turn around  $t=4$  s (Fig. 7(a)) and then a "throttle blip" action was taken during the turn, that is, an applied throttle command around  $t=6$  s in between two braking actions around  $t=5$  s and  $t=6.5$  s, respectively; see Fig. 7(b). At the same time when the throttling was applied, the driver turned the steering to the cornering direction aggressively and turned it back around  $t=9$  s after the second brake command. As a result of load shifting and rapidly changing  $\lambda$  (Fig. 6(d)) and  $\alpha$  (Fig. 6(e)), large lateral tire/road frictions are generated at right-side tires, while very small forces at left-side tires (Fig. 6(b)). Thus, it produces a large vehicle side-slip angle  $\beta$  (Fig. 6(e)) around  $t=8$  s.

For the highly dynamic pendulum-turn maneuver, we try to generate the vehicle motion in CARSIM simulation using the racing car driver's inputs. The hybrid tire/road friction model is used in the CARSIM simulation to capture dynamically changing tire friction forces. Figure 8 shows an example of the CARSIM simulation comparison results of the longitudinal and the lateral velocity/acceleration, the yaw rate, and the vehicle side-slip angle. The simulation results shown in Fig. 8 match well with the testing data. We also observed the similar matching results for other motion and force variables. These simulation results confirm that the hybrid tire/road friction model accurately predicts vehicle motion under dynamically changing conditions.

## 6 Conclusion and Future Work

We presented an integrated physical-dynamic tire/road friction model for vehicle dynamics simulation and control applications. We took advantages of the attractive properties of both the physical and the dynamic friction models in the proposed modeling framework. The new model integrated the contact patch partition from the physical friction model with the normal load-dependent bristle deformation calculation from the LuGre dynamic friction model. Such a model integration resolved the issue of the unrealistic nonzero deformation at the trailing edge of the contact patch that was reported by other dynamic friction models. The hybrid modeling approach also bridged the connection of the physical model parameters with those of the LuGre dynamic models. Finally, we demonstrated one application example of the use of the hybrid friction model to capture rapidly changing tire dynamics in a pendulum-turn aggressive vehicle maneuver.

We currently extend the presented work in several directions. We are building and testing a single-wheel distributed "smart tire" sensing systems to enhance and validate the modeling developments. Real-time control of autonomous aggressive vehicle maneuvers using the hybrid tire/road friction model is also among the ongoing work.

## Acknowledgment

The authors thank Dr. W. Liang, Dr. J. Lu, and Dr. E. H. Tseng of Ford Research & Innovation Center for their helpful discussions and suggestions.

The authors are grateful to Professor P. Tsotras of Georgia Institute of Technology (USA) and Dr. E. Velenis of Brunel University (UK) for sharing of the testing data for the pendulum-turn aggressive vehicle maneuvers. This work was supported in part by the US National Science Foundation under Grant CMMI-0856095 and CAREER award CMMI-0954966 (J. Yi) and a fellowship from the Chinese Scholarship Council (J. Li).

## Appendix A: Proof of Property 2

By definition, the contact patch separation location  $x_c$  is given by solving  $\sigma_a(x) = \sigma_s(x)$ . From Eqs. (19)–(21), we obtain that  $x_c$  is the root of Eq. (31) for a given  $x_a > 0$ . Noting that  $h(0; x_a) = 0$ ,  $h(1; x_a) = z_l \hat{\sigma}_0 / 6g(v_R) > 0$  and  $h'(0; x_a) = dh/dx|_{x=0} = 0$ , we conclude that there exists at least one *nontrivial* root  $0 < x_c < 1$  for equation  $h(x; x_a) = 0$  due to the continuity of function  $h(x; x_a)$ . Moreover, we find that the solution can be written in a form of the Lambert W function of  $x_a$  as (35). Noting  $X_a = (-x_a/2 - 1)e^{(-x_a/2)-1}$ , we obtain

$$\frac{dX_a}{dx_a} = \frac{x_a}{2} e^{-\frac{x_a}{2}-1} \geq 0$$

for  $x_a \geq 0$ . Thus,  $X_a$  is monotonically increasing with  $x_a$  and  $-e^{-1} \leq X_a < 0$ . Using the property of the Lambert W function  $-1 \leq W_0(X_a) < 0$  for  $-e^{-1} \leq X_a < 0$ ,  $x_c$  satisfies

$$x_c = \frac{1}{2} + \frac{W_0(X_a) + 1}{x_a} \geq \frac{1}{2}$$

From the definition of the Lambert W function  $x = W(z)$  (i.e., solution of  $z = xe^x$ ), we have

$$z[1 + W(z)] \frac{dW}{dz} = W(z)$$

for  $z \neq -e^{-1}$ , and thus obtains

$$W'(z) = \frac{dW}{dz} = \frac{W(z)}{z[1 + W(z)]}, \quad \text{for } z \neq 0, -e^{-1} \quad (\text{A1})$$

We further calculate

$$\frac{dx_c}{dx_a} = \frac{W'_0(X_a) \frac{dX_a}{dx_a} x_a - [1 + W_0(X_a)]}{x_a^2} = -\frac{f(x_a)}{x_a^2(x_a + 2)[1 + W_0(X_a)]} \quad (\text{A2})$$

where  $f(x_a) = x_a^2 W_0(X_a) + [1 + W_0(X_a)]^2(x_a + 2)$ . Note that  $f(0) = 0$ , and

$$f'(x_a) = \frac{-x_a^3 W_0(X_a)}{(x_a + 2)[1 + W_0(X_a)]} + [1 + W_0(X_a)]^2 > 0$$

since  $W_0(X_a) < 0$  for a finite  $x_a > 0$ . Therefore,  $f(x_a) \geq 0$  for  $x_a \geq 0$ . From (A2), we conclude that  $x_c$  is a monotonically decreasing function of  $x_a$ .

It is straightforward to see that  $x_c \rightarrow 1/2$  as  $x_a \rightarrow \infty$  from Eq. (35) since  $W_0(X_a) + 1$  is bounded. To calculate  $\lim_{x_a \rightarrow 0} x_c$ , we use the second formulation in Eq. (35)

$$\begin{aligned} \lim_{x_a \rightarrow 0} x_c &= \lim_{X_a \rightarrow -e^{-1}} \left[ \frac{1}{2} - \frac{1}{2} \frac{W_0(X_a) + 1}{W_{-1}(X_a) + 1} \right] \\ &= \frac{1}{2} - \frac{1}{2} \lim_{X_a \rightarrow -e^{-1}} \frac{W_0(X_a) + 1}{W_{-1}(X_a) + 1} \end{aligned} \quad (\text{A3})$$

Note that as  $X_a = -e^{-1}$ ,  $W_0(X_a) = W_{-1}(X_a) = -1$  and, therefore we calculate the above limit by using the derivative of the Lambert W function  $W(z)$ . Taking the derivative of (A1) and using (A1) again, we obtain the second derivative of  $W(z)$  as

$$\frac{d^2W}{dz^2} = -\frac{1}{z(1+W(z))} \frac{dW}{dz} \left(1 + z \frac{dW}{dz}\right) = -\frac{W(z)[2W(z)+1]}{z^2[1+W(z)]^3} \quad (\text{A4})$$

Due to the continuity and monotonicity of the function  $x_c$  on  $x_a$ , we conclude that  $\lim_{x_a \rightarrow -e^{-1}} x_c$  exists. We denote  $L_c = \lim_{x_a \rightarrow -e^{-1}} W_0(X_a) + 1/W_{-1}(X_a) + 1$  and obtain  $L_c < 0$  since  $-1 \leq W_0(X_a) < 0$  and  $W_{-1}(X_a) \leq -1$ . Moreover, we obtain

$$\begin{aligned} L_c &= \lim_{x_a \rightarrow -e^{-1}} \frac{W_0(X_a) + 1}{W_{-1}(X_a) + 1} = \lim_{x_a \rightarrow -e^{-1}} \frac{W_0(X_a)}{W_{-1}(X_a)} \frac{W'_{-1}(X_a)}{W'_0(X_a)} \\ &= \lim_{x_a \rightarrow -e^{-1}} \frac{W''_{-1}(X_a)}{W''_0(X_a)} = \lim_{x_a \rightarrow -e^{-1}} \frac{[W_0(X_a) + 1]^3}{[W_{-1}(X_a) + 1]^3} \\ &= \left[ \lim_{x_a \rightarrow -e^{-1}} \frac{W_0(X_a) + 1}{W_{-1}(X_a) + 1} \right]^3 = L_c^3 \end{aligned} \quad (\text{A5})$$

where in the above calculation, we use the results in (A4). From (A5), we have  $L_c(L_c^2 - 1) = 0$  and thus the nontrivial solution  $L_c = -1$  because of  $L_c < 0$ . From Eq. (A3), we finally obtain

$$\lim_{x_a \rightarrow 0} x_c = \frac{1}{2} - \frac{1}{2}L_c = \frac{1}{2} + \frac{1}{2} = 1$$

This completes the proof of Property 2.

## Appendix B: Proof of Property 3

From the proof of Property 2, we know that there exists an  $x_c$  such that it partitions  $\mathcal{P}$  into the adhesion and sliding regions. With the definition of function  $h(x, x_a)$  in Eq. (16) and the existence of  $x_c$ , to prove the property, it is equivalent to show that for any  $0 \leq x \leq x_c$ ,  $h(x; x_a) \leq 0$  while for  $x_c < x \leq 1$ ,  $h(x; x_a) \geq 0$  for any given  $0 < x_a < +\infty$ .

By the definition of  $x_c$  and (16), we have

$$h(0; x_a) = h(x_c; x_a) = 0 \quad (\text{B1})$$

for any given  $x_a > 0$ . Let  $x_\delta = x - x_c$  denote the variation around  $x_c$ . We define the difference function

$$\begin{aligned} h_\delta &= h_\delta(x; x_c, x_a) = h(x; x_a) - h(x_c; x_a) \\ &= \frac{1}{x_a} \left[ 2x_\delta - \left(1 + \frac{2}{x_a}\right) e^{-x_a x_c} (1 - e^{-x_a x_\delta}) \right] \end{aligned} \quad (\text{B2})$$

It is noted that  $h_\delta$  is a continuous function of  $x_\delta$ . Taking the derivative of  $h_\delta$  with respect to  $x_\delta$  and using the equality  $h(x_c; x_a) = 0$ , we obtain

$$\begin{aligned} \frac{dh_\delta}{dx_\delta} &= \frac{1}{x_a} [2 - (2 + x_a) e^{-x_a x_c} e^{-x_a x_\delta}] \\ &= \frac{1}{x_a} [2(1 - e^{-x_a x_\delta}) + x_a(2x_c - 1) e^{-x_a x_\delta}] > 0 \end{aligned}$$

for  $x_\delta > 0$ , that is,  $x_c < x \leq 1$ . Here, we use the conclusion  $x_c > \frac{1}{2}$  from Property 2. Therefore,  $h_\delta$  is a strictly monotonically increasing function of  $x_\delta$ . We then obtain that  $h(x; x_a) > h(x_c; x_a) = 0$  for  $x_c < x \leq 1$ .

To prove  $h(x; x_a) < h(x_c; x_a) = 0$  for  $0 < x \leq x_c$ , we take the derivative of  $h_\delta$  twice and obtain

$$\frac{d^2h_\delta}{dx_\delta^2} = (2 + x_a) e^{-x_a x_c} e^{-x_a x_\delta} > 0$$

for  $x_\delta < 0$  and  $x_a > 0$ . Therefore, function  $h_\delta$  is convex in  $x_\delta$ . From Eqs. (B1) and (B2), we have

$$h_\delta(0; x_c, x_a) = h_\delta(x_c; x_c, x_a) = 0$$

For any  $x \in [0, x_c]$ , we can write  $x = \alpha \cdot 0 + (1 - \alpha)x_c$  for some  $\alpha \in [0, 1]$  and by convexity, we obtain

$$h_\delta(x; x_c, x_a) < \alpha h_\delta(0; x_c, x_a) + (1 - \alpha) h_\delta(x_c; x_c, x_a) = 0$$

It is noted that due to the strict monotonicity of function  $h_\delta$  in  $(x_c, 1]$  and strict convexity in  $[0, x_c]$ , we conclude the uniqueness of  $x_c$ .

To prove that at  $x_{\max} = x_c$ , steady-state deformation  $\delta z_{ss}$  achieves its maximum value, we calculate  $x_{\max}$  at which the adhesion- and sliding-region deformations (22) achieve their maximum values. For the adhesion region, from Eq. (15), we obtain

$$\begin{aligned} \frac{d\delta z_{ss}}{dx} &= \frac{6g(v_R)}{\hat{\sigma}_0} \left[ -2x + \left(1 + \frac{2}{x_a}\right) (1 - e^{-x_a x}) \right] \\ &= -\frac{6g(v_R)}{\hat{\sigma}_0} x_a h(x; x_a) \end{aligned}$$

It is then straightforward to obtain that at  $x_{\max} = x_c$ ,  $d\delta z_{ss}/dx = 0$ . Moreover, from the above calculations, we have  $d\delta z_{ss}/dx > 0$  for  $0 \leq x \leq x_c$ , and  $d\delta z_{ss}/dx < 0$  for  $x_c \leq x \leq 1$ . Therefore,  $x_c$  is the maximum point of function  $\delta z_{ss}(x)$ . Since the sliding-region deformation  $\delta z_{ss}(x) = (6g(v_R)/\hat{\sigma}_0)(-x^2 + x)$  is an decreasing function of  $x \in [x_c, 1]$ , we conclude that at  $x_{\max} = x_c$ , the combined deformation  $\delta z_{ss}(x)$  achieves its maximum value. This completes the proof of Property 3.

## Appendix C: Proof of Property 4

From Eqs. (35) and (38), the relationship of  $x_c \geq x_c^p$  is equivalent to the following inequality

$$\frac{W_0(X_a) + 1}{x_a} \geq \frac{1}{2} - \frac{1}{3}x_a \quad (\text{C1})$$

We define  $\psi_1(x_a) = (W_0(X_a) + 1/x_a) - 1/2 + 1/3x_a = (6[W_0(X_a) + 1] - 3x_a + 2x_a^2)/6x_a = \psi_2(x_a)/6x_a$ , where  $\psi_2(x_a) = 6[W_0(X_a) + 1] - 3x_a + 2x_a^2$ . Since  $x_a \geq 0$ , we only need to show  $\psi_2(x_a) \geq 0$  to prove (C1). Note that  $\lim_{x_a \rightarrow 0} \psi_1(x_a) = \lim_{x_a \rightarrow 0} \psi_2(x_a) = 0$  and, therefore we only need to consider the case  $x_a > 0$  and to show that  $\psi'_2(x_a) > 0$

$$\begin{aligned} \psi'_2(x_a) &= \frac{6W_0(X_a)}{(-\frac{x_a}{2} - 1)e^{-\frac{x_a}{2}-1}[1+W_0(X_a)]} \frac{x_a}{2} e^{-\frac{x_a}{2}-1} - 3 + 4x_a \\ &= \frac{-6W_0(X_a)x_a}{(x_a + 2)[1+W_0(X_a)]} - 3 + 4x_a \\ &= \frac{[1+W_0(X_a)](4x_a^2 - x_a - 6) + 6x_a}{(x_a + 2)[1+W_0(X_a)]} \end{aligned}$$

Note that from (35),  $0 \leq 1 + W_0(X_a)/x_a \leq 1/2$ , namely,  $x_a \geq 2[1 + W_0(X_a)]$ . Thus, from the above equation we obtain

$$\begin{aligned}\psi_2'(x_a) &\geq \frac{[1 + W_0(X_a)](4x_a^2 - x_a - 6) + 12[1 + W_0(X_a)]}{(x_a + 2)[1 + W_0(X_a)]} \\ &= \frac{4x_a^2 - x_a + 6}{x_a + 2} = \frac{4(x_a - \frac{1}{8})^2 + 5\frac{15}{16}}{x_a + 2} > 0\end{aligned}$$

$\psi_2(x_a) > 0$  for  $x_a > 0$  because of  $\psi_2'(x_a) > 0$  and  $\psi_2(0) = 0$ . We obtain  $\psi_1(x_a) \geq 0$  and this completes the proof.

## References

- [1] Rajamani, R., Piyabongkarn, D., Lew, J. Y., Yi, K., and Phanomchoeng, G., 2010, "Tire-Road Friction-Coefficient Estimation," *IEEE Control Syst. Mag.*, **30**(4), pp. 54–69.
- [2] Gruber, S., Semsch, M., Strothjohann, T., and Breuer, B., 2002, "Elements of a Mechatronic Vehicle Corner," *Mechatronics*, **12**(8), pp. 1069–1080.
- [3] Müller, S., Uchanski, M., and Hedrick, K., 2003, "Estimation of the Maximum Tire-Road Friction Coefficient," *ASME J. Dyn. Syst., Meas., Control*, **125**(4), pp. 607–617.
- [4] Yi, J., 2008, "A Piezo-Sensor Based "Smart Tire" System for Mobile Robots and Vehicles," *IEEE/ASME Trans. Mechatron.*, **13**(1), pp. 95–103.
- [5] Bakker, E., Nyborg, L., and Pacejka, H. B., 1987, "Tyre Modelling for Use in Vehicle Dynamics Studies," SAE Technical Paper No. 870421, pp. 190–204.
- [6] Pacejka, H. B., 2006, *Tire and Vehicle Dynamics*, 2nd ed., SAE International, Warrendale, PA.
- [7] Gim, G., and Nikravesh, P., 1990, "An Analytical Model of Pneumatic Tyres for Vehicle Dynamic Simulations. Part I: Pure Slips," *Int. J. Veh. Des.*, **11**(6), pp. 589–618.
- [8] Fancher, P., and Bareket, Z., 1992, "Including Roadway and Tread Factors in a Semi-Empirical Model of Truck Tyres," *Veh. Syst. Dyn.*, **21**(Suppl.), pp. 92–107.
- [9] Wong, J. Y., 2001, *Theory of Ground Vehicles*, 3rd ed., John Wiley & Sons, Inc., Hoboken, NJ.
- [10] Fancher, P., Bernard, J., Clover, C., and Winkler, C., 1997, "Representing Truck Tire Characteristics in Simulations of Braking and Braking in Turn Maneuvers," *Veh. Syst. Dyn.*, **27**(Suppl.), pp. 207–220.
- [11] Svendenius, J., 2007, "Tire Modeling and Friction Estimation," Ph.D. dissertation, Department of Automatic Control, Lund Institute of Technology, Lund, Sweden.
- [12] Bliman, P., Bonald, T., and Sorine, M., 1995, "Hysteresis Operators and Tyre Friction Models: Application to Vehicle Dynamic Simulation," Proceedings of ICIAM, Hamburg, Germany.
- [13] Yi, J., Alvarez, L., Claeys, X., and Horowitz, R., 2003, "Tire/Road Friction Estimation and Emergency Braking Control Using a Dynamic Friction Model," *Veh. Syst. Dyn.*, **39**(2), pp. 81–97.
- [14] Alvarez, L., Yi, J., Olmos, L., and Horowitz, R., 2005, "Adaptive Emergency Braking Control With Observer-Based Dynamic Tire/Road Friction Model and Underestimation of Friction Coefficient," *ASME J. Dyn. Syst., Meas., Control*, **127**(1), pp. 22–32.
- [15] Canudas de Wit, C., Tsiotras, P., Velenis, E., Basset, M., and Gissinger, G., 2003, "Dynamic Friction Models for Road/Tire Longitudinal Interaction," *Veh. Syst. Dyn.*, **39**(3), pp. 189–226.
- [16] Deur, J., Asgari, J., and Hrovat, D., 2004, "A 3D Brush-Type Dynamic Tire Friction Model," *Veh. Syst. Dyn.*, **42**(3), pp. 133–173.
- [17] Velenis, E., Tsiotras, P., Canudas de Wit, C., and Sorine, M., 2005, "Dynamic Tyre Friction Models for Combined Longitudinal and Lateral Vehicle Motion," *Veh. Syst. Dyn.*, **43**(1), pp. 3–29.
- [18] Koo, S.-L., and Tan, H.-S., 2007, "Dynamic-Deflection Tire Modeling for Low-Speed Vehicle Lateral Dynamics," *ASME J. Dyn. Syst., Meas., Control*, **129**(3), pp. 393–403.
- [19] Liang, W., Medanic, J., and Ruhl, R., 2008, "Analytical Dynamic Tire Model," *Veh. Syst. Dyn.*, **46**(3), pp. 197–227.
- [20] Tyukin, I., Prokhorov, D., and van Leeuwen, C., 2005, "A New Method for Adaptive Brake Control," Proceedings of the American Control Conference, Portland, OR, pp. 2194–2199.
- [21] Yi, J., 2009, "On Hybrid Physical/Dynamic Tire-Road Friction Model," Proceedings of the ASME Dynamic Systems and Control Conference, Hollywood, CA, Paper No. DSCC2009-2548.
- [22] Yi, J., Li, J., Lu, J., and Liu, Z., 2012, "On the Dynamic Stability and Agility of Aggressive Vehicle Maneuvers: A Pendulum-Turn Maneuver Example," *IEEE Trans. Control Syst. Technol.*, **20**(3), pp. 663–676.
- [23] Haessig, D. A., Jr., and Friedland, B., 1991, "On the Modeling and Simulation of Friction," *ASME J. Dyn. Syst., Meas., Control*, **113**(3), pp. 354–362.
- [24] Corless, R. M., Gonnet, G. H., Hare, D. E. G., Jeffrey, D. J., and Knuth, D. E., 1996, "On the Lambert W Function," *Adv. Comput. Math.*, **5**, pp. 329–359.
- [25] Yi, J., and Tseng, E. H., 2009, "Nonlinear Analysis of Vehicle Lateral Motions With a Hybrid Physical/Dynamic Tire-Road Friction Model," Proceedings of the ASME Dynamic Systems and Control Conference, Hollywood, CA, Paper No. DSCC2009-2717.
- [26] O'Neil, T., 2006, *Rally Driving Manual*, Team O'Neil Rally School and Car Control Center, Dalton, NH, <http://www.team-oneil.com/>
- [27] Velenis, E., Tsiotras, P., and Lu, J., 2007, "Modeling Aggressive Maneuvers on Loose Surface: The Cases of Trail-Braking and Pendulum-Turn," Proceedings of the European Control Conference, Kos, Greece, pp. 1233–1240.
- [28] Yi, J., Wang, H., Zhang, J., Song, D., Jayasuriya, S., and Liu, J., 2009, "Kinematic Modeling and Analysis of Skid-Steered Mobile Robots With Applications to Low-Cost Inertial Measurement Unit-Based Motion Estimation," *IEEE Trans. Rob.*, **25**(5), pp. 1087–1097.